machines

MDPI

Article

Wiring Network Fault Diagnosis Based on Time-Domain Reflectometry and Gramian Angular Field Encoding with Residual Neural Networks

Abdelhak Goudjil [1,2,*], Mostafa Kamel Smail [1,2], Muhammad Sharjeel Javaid [3] and Houssem Rafik El-Hana Bouchekara [4]

[1] Institut Polytechnique des Sciences Avancees (IPSA), 63 Boulevard de Brandebourg, 94200 Ivry-sur-Seine, France; mostafa-kamel.smail@ipsa.fr
[2] Group of Electrical Engineering Paris (GeePs), UMR CNRS 8507, CentraleSupelec, Université Paris-Saclay, Sorbonne University, 11 Rue Joliot Curie, 91192 Gif-sur-Yvette, France
[3] Department of Electrical and Electronic Engineering, Imperial College London, London SW7 2AZ, UK
[4] Department of Electrical Engineering, University of Hafr Al Batin, Hafr Al Batin 31991, Saudi Arabia
* Correspondence: abdelhak.goudjil@ipsa.fr

Abstract

This paper introduces a novel fault diagnosis framework for wiring networks that integrates Time Domain Reflectometry (TDR) with Gramian Angular Field (GAF) representations and a deep residual neural network. The proposed methodology transforms TDR responses into GAF images, which are directly exploited by the residual neural network to enable robust feature extraction from complex reflectometry signals. To support supervised learning, a forward modeling strategy is employed to generate representative TDR responses under a wide range of fault scenarios. Theframeworkis designed to provide real-time fault detection, localization, and characterization, demonstrating high effectiveness on complex topologies such as the YY-shaped network. Numerical results demonstrate high diagnostic performance for hard faults, achieving an overall accuracy and macro-averaged sensitivity exceeding 99%, thereby highlighting the effectiveness and reliability of the proposed approach.

Keywords: Time Domain Reflectometry; Gramian Angular Fields; residual neuralnetworks; wiring network; diagnosis

Check for updates

Academic Editors: Huitian Lu, Mohammad Omidi and Ali Naderi Bakhtiyari

Received: 13 April 2026
Revised: 31 May 2026
Accepted: 5 June 2026
Published: 9 June 2026

Copyright: © 2026 by the authors. Licensee MDPI, Basel, Switzerland. This article is an open access article distributed under the terms and conditions of the Creative Commons Attribution (CC BY) license.

1. Introduction

Wiring defects represent a major safety concern in critical sectors such as the aerospace, automotive, and nuclear industries. Over time, electrical cables are subjected to aging, mechanical stress, and environmental influences, which can lead to insulation degradation, brittleness, or structural damage, ultimately causing severe system failures. For example, in aircraft, the total length of onboard wiring can reach up to 400 km for a modern airplane, which significantly increases their exposure to mechanical wear, environmental stress, and aging effects, making fault detection particularly challenging. A single undetected defect can have catastrophic consequences, as tragically demonstrated by the accidents of TWA Flight 800 in 1996 and Swissair Flight 111 in 1998 [1]. These events highlight the urgent need for robust diagnostic techniques capable of accurately detecting, locating, and characterizing wiring faults in a timely manner. Wiring faults are generally categorized into hard and soft faults. Hard faults, such as open-circuit or short-circuit conditions, lead

to a sudden and significant degradation of network performance. Soft faults, in contrast, are associated with localized variations in impedance; although initially subtle and difficult to detect, they can gradually worsen and potentially evolve into hard faults, causing major system disruptions. The parameters used to characterize these faults depend on their type. For soft faults, the main focus is on the fault location, the magnitude of impedance changes, and, in some cases, the fault length. Hard faults are described by parameters linked to the physical configuration of the network, including the lengths of affected branches and the connected electrical loads.

Various techniques have been developed for the characterization and localization of wiring faults. These approaches can be broadly divided into two classes. The first class includes non-reflectometry-based methods [2–4], whose main limitation lies in their incompatibility with embedded or onboard applications. The second class covers reflectometry-based techniques. Reflectometry relies on the comparison between an injected signal and its corresponding reflected response, exploiting wave propagation phenomena in physical media [1]. This family of methods mainly includes: time-domain reflectometry (TDR) [1], spectrum-based TDR [5], frequency-domain reflectometry [6], and joint time–frequency reflectometry [7]. In this study, TDR is adopted due to its simplicity of operation, high speed, versatility, and high precision in fault localization. It requires only a single access point while providing rapid and reliable results with precise fault identification, making it well suited for practical applications. TDR responses may be characterized either by means of experimental measurements or by means of modeling and simulation frameworks. In the literature, forward models are widely employed to reproduce measured TDR signals. These models generally fall into two main categories: analytical and numerical approaches [8–11]. Analytical formulations provide closed-form solutions but remain limited when addressing soft or incipient faults, whose detection is hindered by weak and localized impedance variations. In contrast, numerical techniques, such as the Finite-Difference Time-Domain (FDTD) method, offer greater modeling flexibility and are better suited for accurately capturing complex fault behaviors.

Although TDR is a powerful technique for detecting faults in wiring networks, its standalone application is often limited when dealing with complex systems. Subtle impedance variations and intricate network topologies can produce reflection patterns that are difficult to interpret manually or through direct analysis. To overcome these limitations, advanced computational techniques have been developed, which can be broadly classified into two categories: iterative optimization-based methods and machine-learning-based approaches. Iterative optimization methods employ forward models to minimize the discrepancy between measured and simulated TDR responses. In this context, various optimization techniques have been applied, including genetic algorithms [12], particle swarm optimization [13], and reflectometry-based methods combined with statistical analysis [14]. Although these methods are capable of handling complex fault scenarios, they are computationally intensive, sensitive to initialization conditions, and require careful tuning of hyperparameters for different network configurations. Consequently, their convergence times often preclude real-time deployment, and their flexibility for adapting to varying fault types remains limited. In contrast, machine-learning-based approaches adopt a two-stage process comprising offline model training and online real-time diagnostics. During the offline phase, TDR datasets are generated using forward models to construct comprehensive training sets. These data-driven models, which include neural networks [15], support vector machines [16], k-Nearest Neighbor classifier [17], Bidirectional Long Short-Term Memory networks (BiLSTM) [18] and One-Dimensional Convolutional Neural Networks (1D-CNNs) [19], are then trained to map TDR signals to diagnostic outcomes. Once trained, these models offer rapid inference suitable for real-time deployment in onboard moni-

toring systems. Despite their widespread use, these approaches still suffer from notable limitations in both performance and computational efficiency. In particular, conventional machine learning techniques typically rely on hand-made feature extraction, which requires substantial domain knowledge and entails a labor-intensive preprocessing stage. This dependency not only increases development time, but may also restrict the robustness of the resulting models. Moreover, such algorithms often encounter scalability issues when applied to large or high-dimensional datasets, leading to increased computational costs and potentially degraded predictive performance. This limitation becomes even more critical in the context of TDR signals generated from numerical models, where fine spatial discretization produces very large signal vectors. The high dimensionality of these responses represents a major drawback for the inverse diagnostic phase, as it significantly increases the complexity of both training and inference. To mitigate this issue, hybrid approaches combining neural networks with dimensionality reduction techniques such as Principal Component Analysis [20] have been introduced to compress the input data. Although PCA-based compression can considerably reduce signal size and computational requirements, it raises additional challenges, particularly regarding the physical interpretability of the reduced signals and the appropriate selection of the number of principal components.

Although the combination of Gramian Angular Fields (GAF) and Residual Neural Networks (ResNet) is a well-established pipeline in many domains, its potential for TDR remains unexplored. TDR signals exhibit unique physical properties, such as complex spatial reflection echoes, impedance mismatches, and distance-dependent attenuation. Traditional 1D analysis often struggles to capture the subtle long-range correlations between these overlapping echoes in complex wiring networks. To bridge this research gap, this study proposes an original diagnostic framework for wiring networks, in which 1D TDR signals are transformed into 2D GAF representations and subsequently processed using a residual neural network. In contrast to classical optimization-based techniques and conventional machine-learning approaches, the proposed framework offers a number of distinctive advantages, which are summarized as follows.

- Fully automatic feature learning: Taking advantage of deep learning, and in particular residual neural networks, the model automatically extracts discriminative features from GADF representations. By mapping TDR signal properties, such as peak polarity and transient edges, into 2D spatial structures, this approach effectively removes the need for handcrafted feature design and traditional baseline comparisons.
- Robustness to structural complexity through deep residual learning: Thanks to its residual skip connections, the 2D ResNet can train much deeper feature hierarchies without suffering from vanishing gradients, leading to highly abstract and accurate representations. In our context, this capability allows the network to automatically model complex patterns and disentangle the severe overlapping of reflections and topological ambiguities inherent to branched wiring networks, significantly improving overall diagnostic accuracy.
- Strong numerical validation and practical relevance: Instead of proposing a new standalone algorithm, this work introduces a highly effective integration of GADF encoding and ResNet architecture tailored specifically for the complex physics of TDR responses. Comprehensive numerical and hardware evaluations demonstrate a clear and consistent improvement over state-of-the-art methods reported in the literature, satisfy real-time operational constraints, and substantiate the practical relevance of the proposed approach.

This study specifically addresses hard faults, due to their critical influence on the integrity and reliable operation of the network. The remainder of this manuscript is organized as follows. Section 2 introduces the theoretical foundations required to support

the development of the proposed approach. Section 3 details the architecture and main characteristics of the adopted residual neural network. The complete proposed diagnostic framework is then described in Section 4. Section 5 is devoted to the analysis and discussion of the numerical results. Finally, concluding remarks and perspectives are presented in Section 6.

2. Theoretical Backgrounds

2.1. Forward Modeling Approach for Generating TDR Responses

The reflectometry response of a wiring network can be modeled using several strategies reported in the literature, including analytical, semi-analytical, and numerical approaches. In this work, we propose to use a numerical modeling approach designed to accurately capture the electromagnetic behavior of complex wiring networks. The transmission line is discretized into uniform segments of length Δz, each represented by an equivalent elementary RLCG circuit model (R, L, C, and G denote the per-unit-length resistance, inductance, capacitance, and conductance, respectively). By applying Kirchhoff's voltage and current laws to each segment of the network, the multiconductor telegrapher's equations are derived. These equations govern the signal propagation and result in a set of coupled partial differential equations describing the propagation phenomena within the network, which can be expressed as follows:

$$\begin{aligned} \frac{\partial}{\partial z}[V(z,t)] &= -[R]\cdot[I(z,t)] - [L]\cdot\frac{\partial}{\partial t}[I(z,t)] \\ \frac{\partial}{\partial z}[I(z,t)] &= -[G]\cdot[V(z,t)] - [C]\cdot\frac{\partial}{\partial t}[V(z,t)], \end{aligned} \tag{1}$$

where $[V]$ and $[I]$ are column vectors of size $n \times 1$, representing the voltages and currents along the n conductors of the cable. To obtain a numerical solution of the telegrapher's equations, the FDTD method is employed. This technique provides a conceptually straightforward yet powerful framework for modeling electromagnetic wave propagation by discretizing both temporal and spatial variables and approximating differential operators with finite-difference expressions. In many modeling frameworks, transmission lines are assumed to be lossless under specific conditions, so that the resistance R and conductance G may be neglected. Under this lossless assumption, the governing equations reduce to the following simplified form:

$$\begin{aligned} V^{n+1}(z) &= V^{n}(z) - \frac{\Delta t}{C}\cdot\frac{I^{n+1/2}(z+1/2) - I^{n+1/2}(z-1/2)}{\Delta z} \\ I^{n+1/2}(z+1/2) &= I^{n-1/2}(z+1/2) - \frac{\Delta t}{L}\cdot\frac{V^{n}(z+1) - V^{n}(z)}{\Delta z} \end{aligned} \tag{2}$$

To guarantee numerical stability and convergence, the temporal and spatial discretization steps, Δt and Δz, must satisfy the Courant–Friedrichs–Lewy (CFL) condition, which specifies a critical constraint linking these parameters to the characteristic wave propagation velocity [21]. Specifically, the CFL stability condition requires $\Delta t \leq \frac{\Delta z}{v_p}$, where $v_p = \frac{1}{\sqrt{LC}}$ is the phase velocity of the line. A detailed derivation of this condition in the context of TDR-based wiring network modeling can be found in [22]. The accuracy of the forward model is evaluated by comparing a simulated TDR response with an experimentally acquired signal, as shown in Figure 1. The validity of this modeling approach has been rigorously demonstrated in [22], thereby confirming its reliability and predictive accuracy.

It should be noted that the lossless assumption is well justified for the short cable lengths considered in this study (total network length $\approx$ 7.25 m), as verified by the close

agreement between simulated and measured responses shown in Figure 1. For longer cable networks, such as those encountered in aerospace applications, resistive and dielectric losses may become non-negligible, and the integration of frequency-dependent R and G parameters into the forward model would be necessary to ensure accurate predictions.

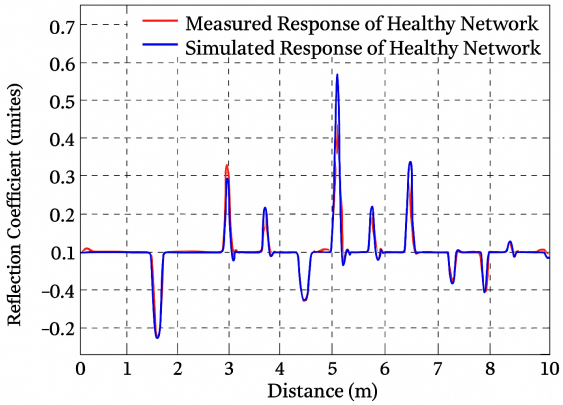


Figure 1. Simulated and experimental TDR signals: comparative analysis.

2.2. TDR Response-to-Image Conversion Using GAF

The GAF representation is a general technique designed to convert one-dimensional signals into two-dimensional images while preserving temporal dependencies and correlations. This method is widely used to enhance the representation of sequential data for visual analysis and machine learning. In this work, the GAF approach is specifically applied to TDR responses, transforming the reflected waveform signals into image-based representations suitable for fault detection and classification. The GAF method includes two variants: the Gramian Angular Summation Field (GASF) and the Gramian Angular Difference Field (GADF). Both rely on mapping the normalized signal into polar coordinates and encoding the relationships between samples in a Gramian matrix. The procedure consists of the following steps.

1. Normalize the TDR response: Let $X = \{x_1, x_2, \ldots, x_n\}$ denote a TDR waveform, where x_i represents the amplitude of the reflected signal at time t_i. The signal is normalized to the interval $[-1, 1]$ as follows:

$$\tilde{x}_i = 2\frac{x_i - \min(X)}{\max(X) - \min(X)} - 1. \tag{3}$$

   Min-max normalization to the $[-1, 1]$ interval is specifically employed rather than Z-score standardization, as it is a strict mathematical prerequisite to satisfy the domain of the arccosine function used in the GADF transformation.
2. Convert to polar coordinates (angular θ_i and radial r_i coordinates): Following the normalization step, each sample is expressed in polar coordinates as

$$\theta_i = \arccos(\tilde{x}_i), \quad -1 \leq \tilde{x}_i \leq 1 \tag{4}$$

$$r_i = t_i / N \tag{5}$$

   where t_i is the time index, N is the total number of samples, and θ_i is the angular coordinate. This transformation combines temporal and amplitude information into a unified representation.

3. Build the Gramian matrices: The Gramian matrix is constructed using the transformed angles. For GASF, the elements are computed as the cosine of the sum of angles:

$$F_{GASF} = \begin{bmatrix} \cos(\theta_1 + \theta_1) & \cos(\theta_1 + \theta_2) & \dots & \cos(\theta_1 + \theta_N) \\ \cos(\theta_2 + \theta_1) & \cos(\theta_2 + \theta_2) & \dots & \cos(\theta_2 + \theta_N) \\ \vdots & \vdots & \ddots & \vdots \\ \cos(\theta_N + \theta_1) & \cos(\theta_N + \theta_2) & \dots & \cos(\theta_N + \theta_N) \end{bmatrix} \quad (6)$$

Similarly, for GADF, the elements are computed as the sine of the difference of angles:

$$F_{GADF} = \begin{bmatrix} \sin(\theta_1 - \theta_1) & \sin(\theta_1 - \theta_2) & \dots & \sin(\theta_1 - \theta_N) \\ \sin(\theta_2 - \theta_1) & \sin(\theta_2 - \theta_2) & \dots & \sin(\theta_2 - \theta_N) \\ \vdots & \vdots & \ddots & \vdots \\ \sin(\theta_N - \theta_1) & \sin(\theta_N - \theta_2) & \dots & \sin(\theta_N - \theta_N) \end{bmatrix} \quad (7)$$

Both representations transform TDR responses into image representations, enabling advanced deep learning applications for cable fault localization and condition monitoring. In this study, we employ the GADF due to its ability to highlight local variations and dynamic transitions in the signal. Unlike GASF, which focuses on global correlations, GADF is significantly more sensitive to polarity changes. This is essential to capture the distinct signature of reflection peaks, allowing the model to capture fine-grained patterns relevant to both fault localization and type characterization. Figure 2 illustrates the complete workflow, from an original TDR response to the final GADF representation. These transformations facilitate the application of advanced deep learning techniques for automated signal analysis and fault characterization.

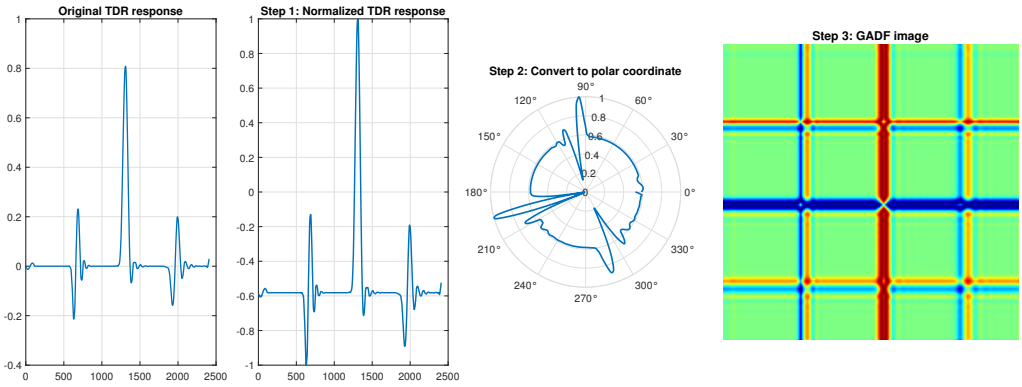


Figure 2. Workflow from TDR response to GADF image.

3. Deep Learning Applications and ResNet Architecture

Recently, data-driven methods and deep learning frameworks have been widely adopted to address complex fault diagnosis issues in various industrial domains. For example, advanced approaches such as federated learning that preserves privacy have been proposed for decentralized fault diagnosis under class-imbalanced conditions [23]. Similarly, deep learning frameworks that combine prior fault frequency have proven highly effective for large-scale systems such as offshore wind turbines [24]. Within this broader context of deep learning, two-dimensional convolutional neural networks are widely utilized in a wide range of application domains, including fault diagnosis [25,26], computer vision [27,28], and healthcare applications [29,30], due to their ability to efficiently extract hierarchical representations while maintaining translation invariance. Several foundational convolutional neural network architectures, most notably AlexNet [31], GoogLeNet [32],

and ResNet [33,34], have been instrumental in driving progress in terms of achievable network depth, representational capacity for hierarchical feature extraction, and overall computational efficiency. In this work, we adopt the ResNet-50 model [35]. ResNet retains the conventional CNN pipeline (input convolution and pooling layers, feature extraction, and prediction) while introducing residual connections designed to mitigate gradient disappearance problems in deep architectures. These skip connections enable information to bypass intermediate layers, thus facilitating stable training and preserving accuracy even when certain layers provide limited contribution. Using ResNet-50 with transfer learning eliminates the need to train from scratch on large labeled datasets, reducing computational cost while enabling faster convergence and better performance, even with limited training data.

For the wiring network diagnosis application studied in this paper, we adopt the ResNet-50 architecture for both the classification and regression tasks. Its overall structure and the key hyperparameters used in each case are illustrated in Figure 3. For classification, the ResNet-50 architecture comprises an initial convolutional stem, four sequential groups of residual bottleneck blocks, a global average pooling layer, a fully connected classifier, and final softmax activation. The input image is first processed by the stem and residual stages, progressively transformed into deeper and more abstract feature representations. Pooling operations reduce spatial resolution while increasing the number of feature channels, thereby enhancing the network's capacity to capture high-level discriminative patterns. The global average pooling layer condenses the final feature map into a one-dimensional vector, which is passed through a fully connected layer. Subsequent softmax activation produces a probability distribution in the fault categories and the class with the highest probability is selected as the predicted fault label. For regression, the ResNet-50 architecture is modified by replacing the global average pooling layer with a flattening layer. This adjustment preserves the complete spatiotemporal and feature information from the last residual block, avoiding the loss of fine-grained temporal dependencies that spatial averaging may remove, an essential aspect for accurate regression. The flattened representation is fed into a fully connected layer with a single output neuron to generate scalar predictions. In contrast to the classification case, no softmax activation is applied; instead, a regression output layer is used. The choice of loss function is task-dependent: categorical cross-entropy for classification and mean squared error for regression.

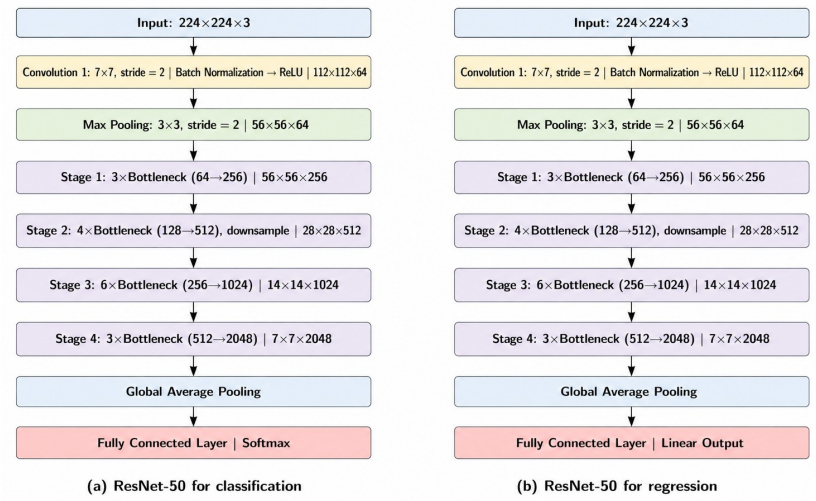


Figure 3. ResNet-50 architectures for classification and regression.

4. The Proposed Methodology

The methodology is structured into a preparatory offline phase and an online processing phase, which are detailed comprehensively in the following subsections.

4.1. Preparatory Offline Phase

The preparatory offline phase, as illustrated in Figure 4, involves generating TDR responses for different wiring network configurations using the forward model and converting these responses into images via GADF. These images are subsequently used to train and validate a set of ResNet-50 models designed for both classification and regression tasks. The key steps of this preparatory offline phase are summarized below.

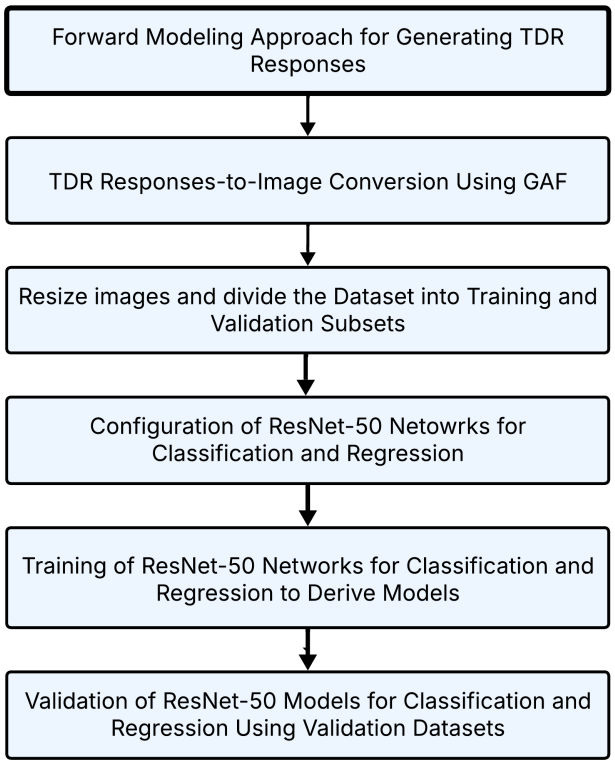


Figure 4. Workflow of the preparatory offline phase.

- Forward modeling for generating TDR responses: The offline phase starts with the use of a forward simulation model to produce synthetic TDR signals. This model emulates the behavior of the wiring network under various operating conditions and possible fault scenarios. The resulting TDR data provide illustrative examples that associate each reflectometry signature with the corresponding fault type, fault location, and the lengths of the impacted branches.
- TDR Response-to-Image Conversion Using GADF: One-dimensional TDR responses are converted into two-dimensional GADF images, which encode the signal's temporal behavior into structured matrices. This visual transformation highlights subtle variations in shape, magnitude, and reflections, enabling downstream image-based learning methods to extract features more effectively and identify complex fault characteristics.
- Resize Images: Resizing the generated images is a crucial step to ensure compatibility with the ResNet-50 architecture, which requires input images formatted as 224×224 pixels. Although this involves downsampling from the original signal length, the potential loss of fine temporal information is mitigated by the oversampled nature of the TDR data. Since the characteristic pulse width of the reflection peaks exceeds the sampling period, even after a preliminary decimation by a factor of two,

the essential diagnostic features remain well-preserved within the structural patterns of the resized 224 × 224 × 3 images. This fixed structure ensures that the model can effectively process the signals during both training and evaluation while leveraging pre-trained weights.

- Training and validation of a ResNet-50 classification model for predicting affected branches and fault types: The classification task aims to identify the affected branches and classify the nature of the faults. Depending on the complexity of the wiring network under test, either a single model or multiple models may be required. In the case of highly complex networks, the overall problem can be divided into several sub-problems, for which a dedicated ResNet-50 model is developed. The training dataset comprises GADF images along with labels specifying the affected branches.
- Training and validation of a multi-output ResNet-50 regression model to estimate the lengths of affected branches: The regression task aims to estimate the locations of the affected branches; therefore, it is necessary to design a multi-output ResNet-50–based regression model. Leveraging the outputs of the ResNet-50 classification model, the corresponding regression model associated with the predicted branch and fault type is then employed to estimate the fault location. The training dataset cnsists of GADF images paired with the lengths of the corresponding branches, as well as labels indicating the affected branches.

Remark 1. *It is important to note that lighter architectures such as ResNet-18 and MobileNetV2 were preliminarily evaluated as alternatives to ResNet-50. However, they were found to be insufficient in achieving the required diagnostic accuracy compared to existing baseline methods for wiring network diagnosis, such as 1D-CNN [19] and BiLSTM [18].*

4.2. Online Phase

The online processing phase implements the inverse-problem framework for diagnosing wiring networks. As illustrated in Figure 5, this phase consists of three core tasks: fault detection, fault localization, and fault characterization. It is applied directly to the wiring network under test to assess its condition and deliver a complete diagnostic through these three steps. The details of each step are provided below.

- Fault detection: This step is performed by comparing the experimentally measured TDR response of the wiring network under test with a reference healthy response generated by the forward model. The comparison uses the RMSE between the two signals. A specific detection threshold, denoted e, is established to classify the state of the network: if the RMSE is below e, the network is deemed healthy; if it exceeds this threshold, the faults are considered present, and further localization and characterization steps are initiated.
- Fault localization and characterization: Upon fault detection, the diagnostic workflow advances to two complementary tasks: (i) identifying the branches affected by the fault and determining its underlying type, and (ii) estimating the fault's position along the corresponding branches with high spatial resolution. These tasks are executed using the ResNet-50 models trained and validated during the preparatory offline phase. Specifically, the classification models are employed to infer both the fault category and the subset of branches involved, whereas the multi-output ResNet-50 regression model is utilized to estimate the fault location along each identified branch. By integrating these classification and regression components into a unified processing pipeline, the proposed framework enables a comprehensive and internally consistent localization and characterization of faults in wiring networks.

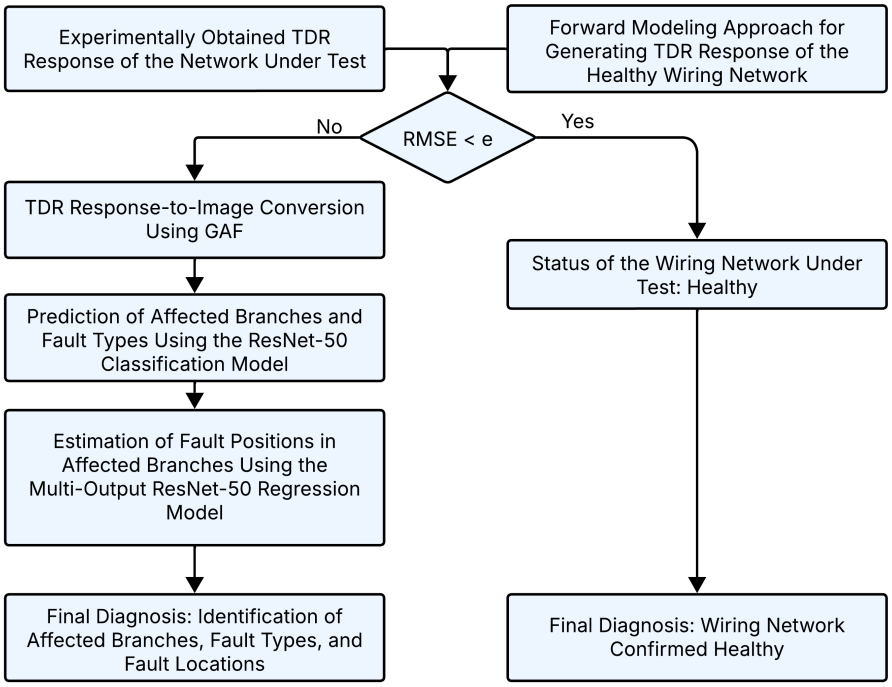


Figure 5. Workflow of the online processing phase.

Remark 2. *It is important to note that the determination criterion for the fault detection threshold e is based mainly on the structural complexity of the network, the modeling errors introduced by the forward model, and the measurement noise present in the experimental TDR responses. As the network structure becomes more complex (for example, transitioning from a Y-network to a YY-network), the baseline RMSE naturally tends to increase. Consequently, a universal threshold cannot be applied. The value of e must be chosen specifically for each structure to be slightly above the maximum RMSE variation caused by inherent structural complexity, forward modeling approximations, and any potential measurement noise. This ensures accurate fault detection while preventing false alarms. For the YY wiring network investigated in the following section, this threshold was established during the experimental validation using the healthy network's response. By calculating the RMSE between the measured and simulated TDR signals under healthy operating conditions, we obtained a baseline value of e = 0.0224. Consequently, any network condition producing an RMSE greater than 0.0224 is classified as faulty, whereas an RMSE equal to or below this threshold indicates normal operation.*

5. Numerical Results

This section examines the YY-shaped wiring network, shown in Figure 6, which consists of five branches with lengths $L_1 = 1.5\,\text{m}$, $L_2 = 1.5\,\text{m}$, $L_3 = 1.5\,\text{m}$, $L_4 = 0.75\,\text{m}$ and $L_5 = 1.5\,\text{m}$. The auxiliary branches are left unterminated (open-circuited) and all conductors are assumed to share identical impedance characteristics. In this investigation, one or two hard faults are introduced to evaluate the performance of the proposed method when applied to a complex network topology. This configuration is used to analyze fault scenarios involving either a single hard fault or two hard faults occurring on distinct branches.

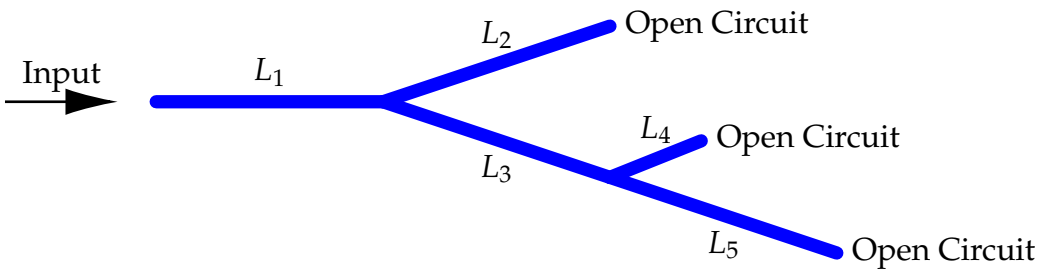


Figure 6. YY-shaped wiring network configuration.

5.1. Offline Training and Performance Evaluation of ResNet-50 Models Using GAF Images Generated from TDR Responses

A dataset for a YY-shaped wiring network with single or double hard faults is constructed using the forward model to simulate the network responses under a wide range of fault scenarios. Each simulation produces a distinct TDR signature associated with a specific fault-condition class. These TDR signals are then converted into labeled GADF images, where each image corresponds to a given TDR response. Each individual GADF image within a specific class represents a distinct, uniquely positioned fault, meaning the total number of images per class reflects the exact number of different physical fault positions considered. For clarity, the study assumes that, when two hard faults occur simultaneously, they are of the same type; however, the proposed diagnostic framework can be straightforwardly extended to handle concurrent faults of different types. For the YY-shaped wiring network, the final labeled dataset comprises 18 classes, each representing a unique fault condition, as detailed below.

- Class L1open: This class corresponds to hard open-circuit faults located at different positions along L_1 and includes 144 GADF images.
- Class L1short: This class corresponds to hard short-circuit faults located at different positions along L_1 and includes 144 GADF images.
- Class L2open: This class corresponds to hard open-circuit faults located at different positions along L_2 and includes 212 GADF images.
- Class L2short: This class corresponds to hard short-circuit faults located at different positions along L_2 and includes 212 GADF images.
- Class L3open: This class corresponds to hard open-circuit faults located at different positions along L_3 and includes 202 GADF images.
- Class L3short: This class corresponds to hard short-circuit faults located at different positions along L_3 and includes 202 GADF images.
- Class L4open: This class corresponds to hard open-circuit faults located at different positions along L_4 and includes 72 GADF images.
- Class L4short: This class corresponds to hard short-circuit faults located at different positions along L_4 and includes 72 GADF images.
- Class L5open: This class corresponds to hard open-circuit faults located at different positions along L_5 and includes 140 GADF images.
- Class L5short: This class corresponds to hard short-circuit faults located at different positions along L_5 and includes 140 GADF images.
- Class L23open: This class corresponds to two simultaneous hard open-circuit faults located on L_2 and L_3 and includes 195 GADF images.
- Class L23short: This class corresponds to two simultaneous hard short-circuit faults located on L_2 and L_3 and includes 195 GADF images.
- Class L24open: This class corresponds to two simultaneous hard open-circuit faults located on L_2 and L_4 and includes 413 GADF images.

- Class L24short: This class corresponds to two simultaneous hard short-circuit faults located on L_2 and L_4 and includes 413 GADF images.
- Class L25open: This class corresponds to two simultaneous hard open-circuit faults located on L_2 and L_5 and includes 236 GADF images.
- Class L25short: This class corresponds to two simultaneous hard short-circuit faults located on L_2 and L_5 and includes 236 GADF images.
- Class L45open: This class corresponds to two simultaneous hard open-circuit faults located on L_4 and L_5 and includes 280 GADF images.
- Class L45short: This class corresponds to two simultaneous hard short-circuit faults located on L_4 and L_5 and includes 280 GADF images.

It should be noted that certain fault combinations are physically impossible in the YY-shaped wiring network. Specifically, any class involving simultaneous faults on the main branch L_1 and on one of its secondary branches (L_2, L_3, L_4, L_5), as well as any class combining a fault on L_3 with a fault on L_4 or L_5, cannot occur. This is due to the fact that a hard fault on L_1 prevents the test signal from propagating to all connected branches, while a hard fault on L_3 blocks signal propagation toward L_4 and L_5.

The dataset is structured to facilitate the training and validation of the ResNet-50 models for both classification and regression tasks. The GADF images data are partitioned into two mutually exclusive subsets: a training set representing 80% of the labeled GADF images and a validation set comprising the remaining 20%. The training configuration adopted for the ResNet-50 models is reported in Table 1. Model hyperparameters are optimized via a grid-search procedure to identify the most effective training configuration. This optimization strategy is designed to improve classification accuracy and regression performance while simultaneously minimizing the corresponding loss functions.

Table 1. Training configuration and hyperparameters for ResNet-50.

Hyperparameter	Value
Training set proportion	80%
Validation set proportion	20%
Optimization algorithm	Adam
Initial learning rate	1×10^{-3}
Maximum number of epochs	256
Mini-batch size	128
Validation interval (epochs)	10
Early stopping patience (epochs)	50
ExecutionEnvironment	gpu
L2Regularization	1×10^{-3}
GradientThreshold	1
OutputNetwork	best-validation

Figure 7 shows the training and validation behavior of the ResNet-50 classification model over iterations. Accuracy (top) and loss (bottom) curves for both sets are closely aligned, indicating stable and consistent learning. The model reaches a high classification accuracy of 99.2%, demonstrating strong generalization. These convergent performance metrics highlight the robustness and reliability of ResNet-50 when using GADF images for wiring network diagnosis.

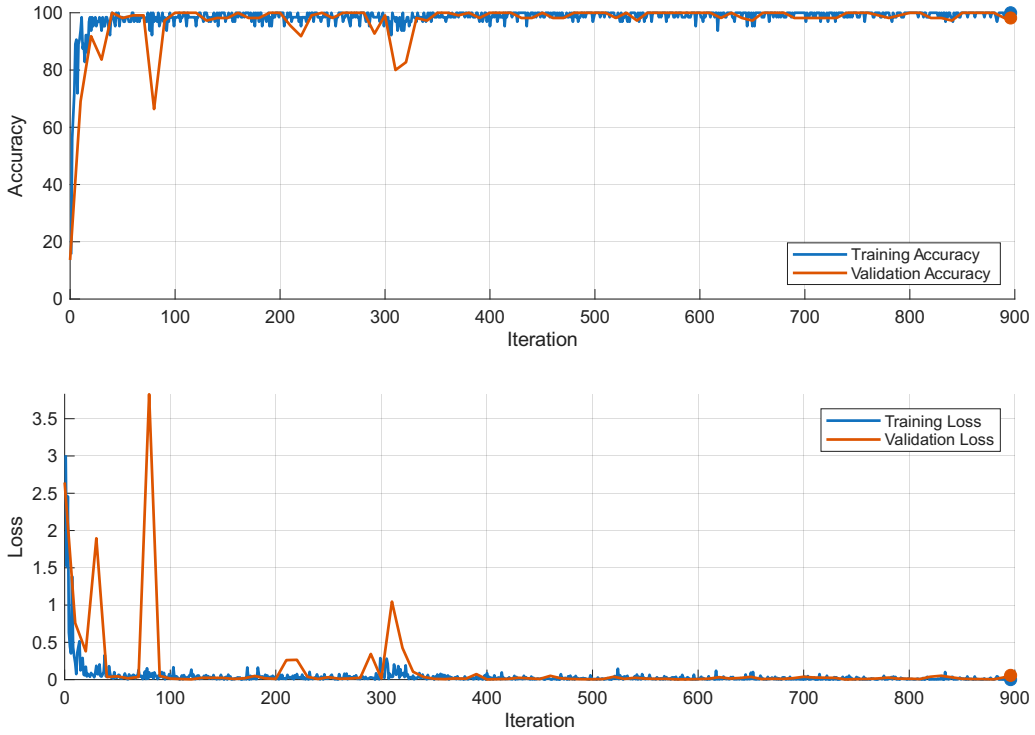


Figure 7. ResNet -50 GADF images classification: evolution of training and validation accuracy, as well as training and validation loss, as a function of the number of iterations.

Figure 8 shows four randomly selected GADF images from the validation set. These GADF images were classified using the trained ResNet-50 model, and the results emphasize the exceptional accuracy and performance of the model.

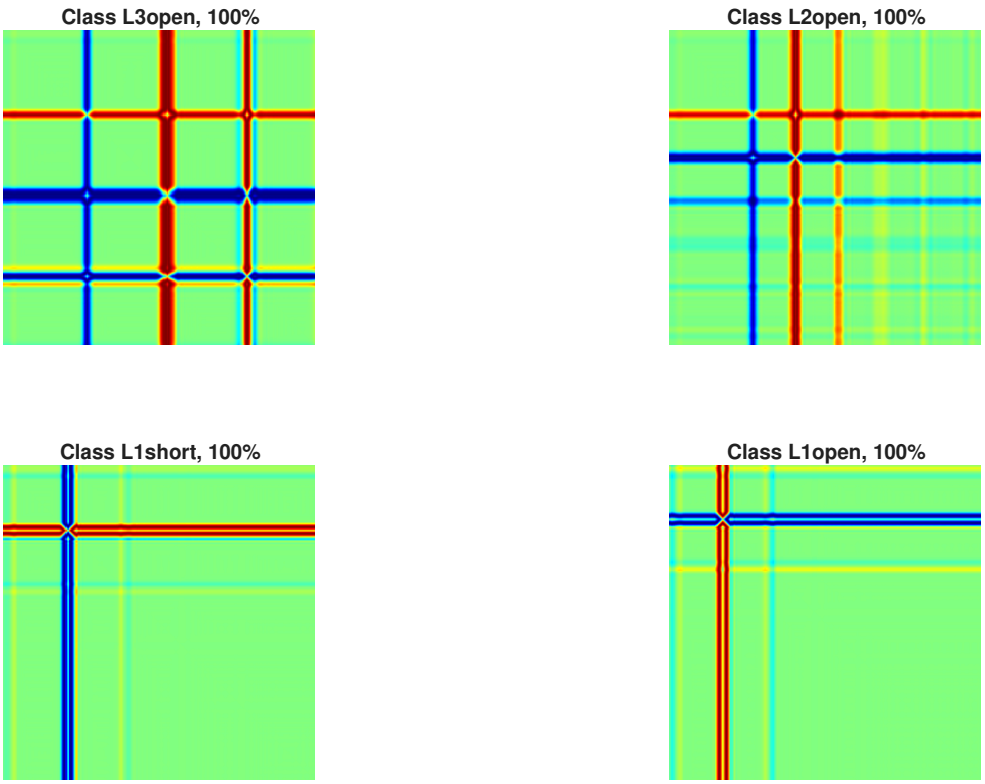


Figure 8. Classification results for four images selected randomly from the validation set.

Figure 9 shows the validation confusion matrix. The model achieves near-perfect classification, demonstrating its ability to accurately capture the temporal patterns of each class.

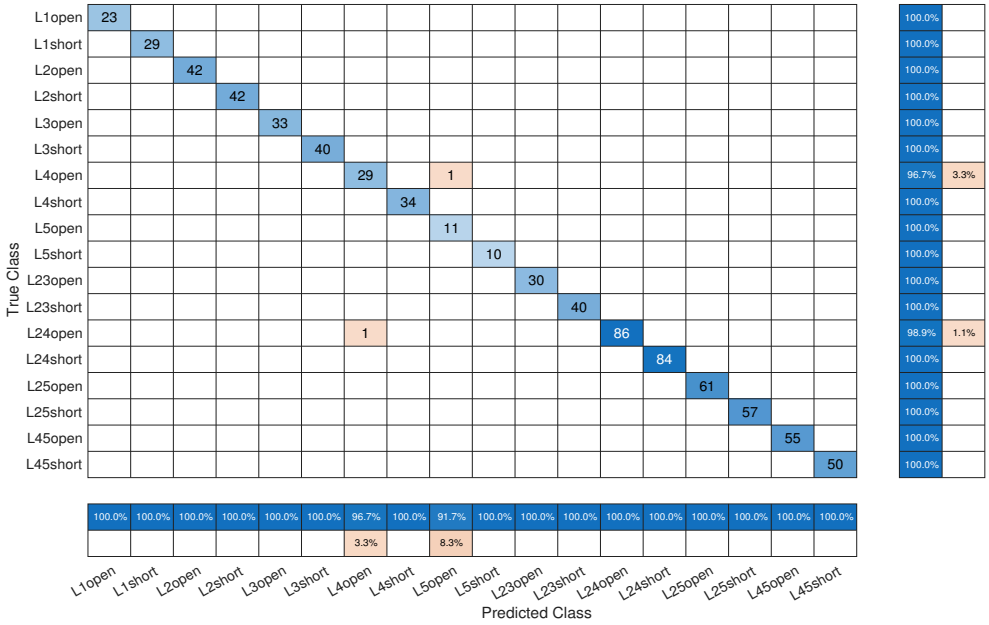


Figure 9. Validation confusion matrix of the ResNet-50 based on GADF representations for the YY-shaped wiring configuration.

To rigorously assess the proposed approach against established deep learning baselines, a comparative study was performed using TDR–1D-CNN [19] and TDR–BiLSTM [18]. Table 2 reports the validation results in terms of overall accuracy, macro-averaged sensitivity, and macro-averaged F1-score, defined as follows:

$$\text{Accuracy (\%)} = \frac{\text{Correct Predictions}}{\text{Total Predictions}} \times 100 \tag{8}$$

$$\text{Macro-Averaged Sensitivity (\%)} = \frac{1}{M}\sum_{i=1}^{M}\text{Sensitivity}_i \times 100 \tag{9}$$

$$\text{Sensitivity}_i(\%) = \frac{\text{True Positives}_i}{\text{True Positives}_i + \text{False Negatives}_i} \times 100 \tag{10}$$

$$\text{Macro-Averaged F1-score (\%)} = \frac{1}{M}\sum_{i=1}^{M}\text{F1-score}_i \times 100 \tag{11}$$

where M denotes the number of classes. Sensitivity measures the proportion of correctly identified instances per class, while the F1-score balances precision and sensitivity to provide a robust performance measure. For each model, the dataset was randomly split into training and validation subsets, and the procedure was repeated over ten independent runs to ensure statistical reliability. The results consistently demonstrate the superior generalization and classification performance of the proposed method for all considered fault conditions.

Table 2. Comparison of the proposed method with baseline approaches in terms of classification performance: accuracy, macro-averaged sensitivity, and macro-averaged F1-score.

Method	Accuracy (%)	Macro-Avg Sens. (%)	Macro-Avg F1 (%)
Proposed Method	99.12 ± 0.22	98.10 ± 0.52	97.96 ± 0.59
TDR–1D-CNN [19]	98.52 ± 0.25	97.87 ± 0.57	97.34 ± 0.61
TDR–BiLSTM [18]	98.30 ± 0.29	97.80 ± 0.59	97.13 ± 0.63

For the regression task, a multi-output ResNet-50 model was developed to estimate fault positions across all labeled classes. For classes corresponding to single-fault scenarios, the model produces one continuous output per class, whereas for classes involving two simultaneous faults, two continuous outputs are generated accordingly. The input of the model consists of the GADF images associated with each branch fault configuration, together with the corresponding continuous fault locations and class identifiers. Following the classification task, the regression outputs are generated only for the class identified by the classifier, ensuring that each prediction is conditioned on the detected fault class. The dataset was partitioned into training (80%) and validation (20%) subsets to ensure robust model development. Regression training of the multi-output ResNet-50 was conducted under conditions consistent with those adopted for the classification task, with an extensive hyperparameter tuning phase performed using a grid-search strategy to identify the optimal training configuration.

Figure 10 illustrates predicted-versus-actual fault locations for four representative regression outputs. These outputs correspond to open circuit faults on branches L_1 and L_3, as well as short circuit faults on branches L_2 and L_4, evaluated at multiple positions. Although the scatter plots for the remaining fault classes are omitted for conciseness, a comprehensive quantitative assessment of the localization performance is detailed in Table 3. This table reports the RMSE across all 18 single and double fault classes. Overall, these results indicate a high level of accuracy, with predicted fault positions closely matching ground-truth values. Once trained, this multi-output model can be directly applied in real-time diagnostic scenarios, enabling reliable fault localization across all classes within a wiring network under test.

Table 3. RMSE regression outputs (in meters) and their standard deviations over ten independent runs for single and double faults.

Single Faults		Double Faults		
Class	**RMSE ± SD (m)**	**Class**	**$RMSE_1$ ± SD (m)**	**$RMSE_2$ ± SD (m)**
Class 1	0.0002 ± 0.00003	Class 11	0.015 ± 0.002	0.017 ± 0.002
Class 2	0.0002 ± 0.00002	Class 12	0.019 ± 0.003	0.016 ± 0.002
Class 3	0.031 ± 0.004	Class 13	0.011 ± 0.001	0.012 ± 0.001
Class 4	0.026 ± 0.003	Class 14	0.013 ± 0.002	0.015 ± 0.002
Class 5	0.0018 ± 0.0002	Class 15	0.016 ± 0.002	0.014 ± 0.001
Class 6	0.0015 ± 0.0001	Class 16	0.012 ± 0.001	0.011 ± 0.002
Class 7	0.0028 ± 0.0003	Class 17	0.015 ± 0.002	0.014 ± 0.002
Class 8	0.0025 ± 0.0002	Class 18	0.014 ± 0.001	0.013 ± 0.001
Class 9	0.012 ± 0.001			
Class 10	0.014 ± 0.002			

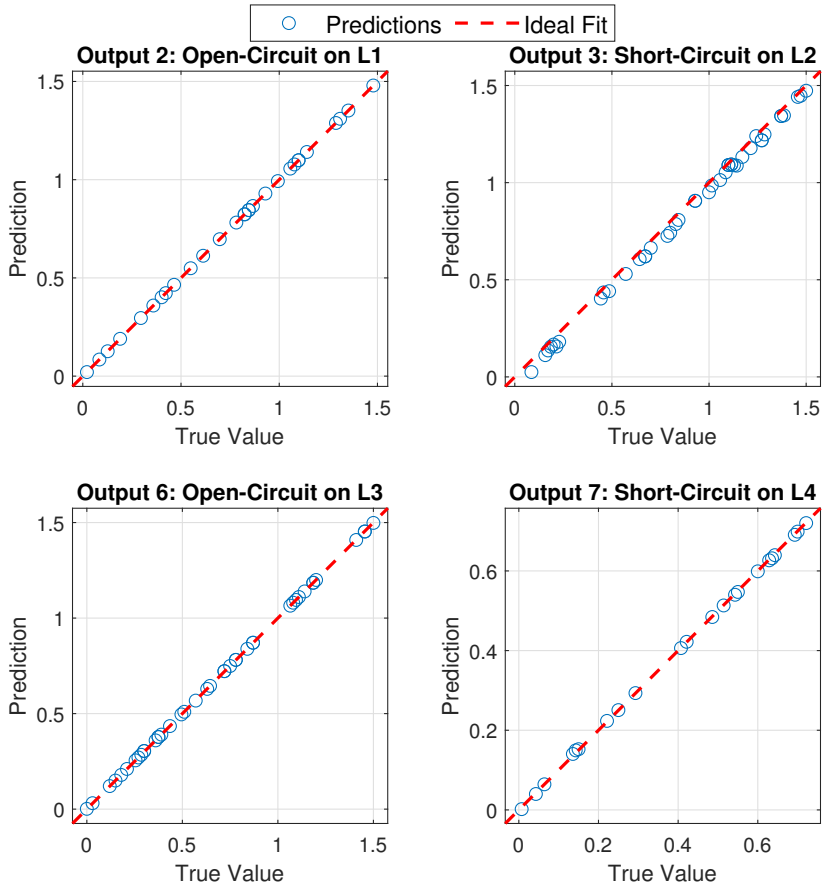


Figure 10. Regression performance of the multi-output ResNet-50 for four representative outputs.

Remark 3. *To evaluate the performance of the proposed method under more realistic measurement conditions, Gaussian noise was added to the simulated TDR signals at three different SNR levels: 40 dB, 30 dB, and 20 dB. The lowest SNR corresponds to a particularly challenging environment, representative of strong electromagnetic interference or significant signal degradation along long cable lengths. Despite the added noise, the method maintained a high level of performance, achieving classification accuracies of 98.5%, 97.2%, and 93.1%, respectively. Even at 20 dB SNR, the reduction in accuracy remained below 6% compared with the noise-free case, which is acceptable for practical fault diagnosis applications. These results demonstrate that the proposed approach is not only effective under ideal simulation conditions but also sufficiently robust to cope with the levels of noise typically encountered in real-world cable diagnostic systems.*

5.2. Online Phase: Diagnosis of the Wiring Network Under Test

An experimental YY-shaped wiring network is investigated, in which two branches are affected by hard faults. The experimental TDR measurement is performed using the setup depicted in Figure 11. An Agilent Technologies E5071C Vector Network Analyzer is employed, operating in the frequency domain over a bandwidth ranging from 100 kHz to 4.5 GHz. The frequency-domain S11 data acquired by the VNA were converted to an equivalent time-domain TDR trace using an IFFT-based procedure. The S11 spectrum was conjugate-symmetrized, zero-padded to the next power of two, and transformed via IFFT. The distance axis was derived using a propagation velocity $v = 0.826c$, consistent with the cable parameters of the experimental setup. A representative faulty configuration is illustrated in Figure 12a, where defects are located on branches L_2 and L_5. Figure 12b compares the measured TDR responses of the healthy and faulty networks. It should be noted that the current experimental validation is restricted to this single faulty configu-

ration due to the practical constraints of manually reconfiguring the physical network. Consequently, conducting broader experimental campaigns is left for future work.

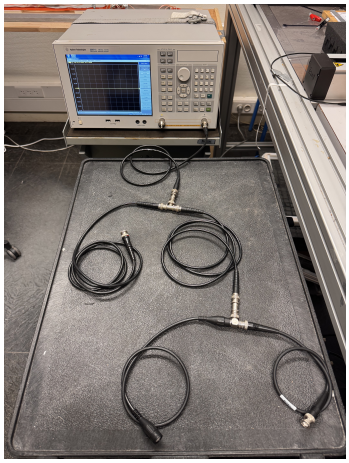


Figure 11. The experimental setup to obtain measurements experimentally.

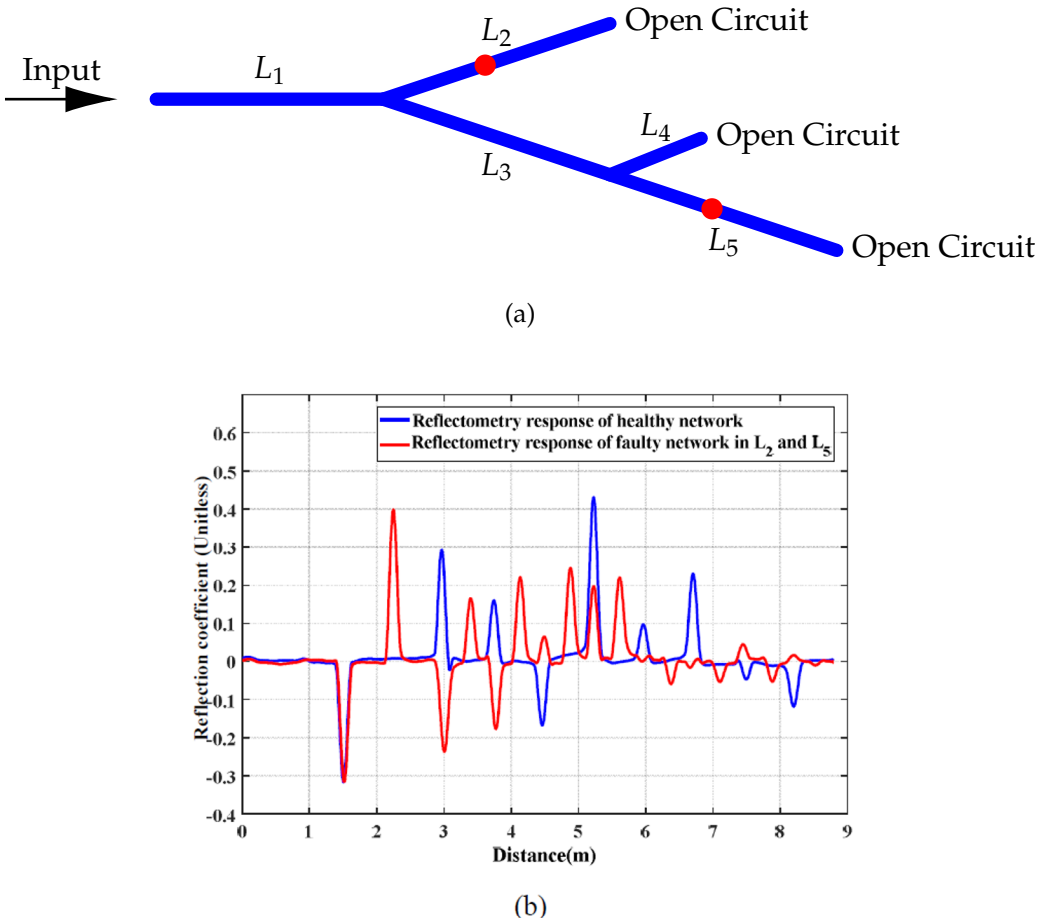


Figure 12. (**a**) YY-shaped wiring network with hard faults applied to branches L_2 and L_5; (**b**) comparative TDR responses of the healthy and faulted networks.

Initially, the RMSE is computed to compare the experimentally measured TDR response of the wiring network under test with the reference response of a healthy network. The RMSE obtained exceeds the predefined threshold, confirming the presence of a fault and completing the detection stage of the online diagnostic procedure. The online phase then proceeds with fault localization and characterization.

To identify the defective branches and determine the nature of the faults, the online diagnostic workflow, based on the ResNet-50 classification model developed and trained during the offline preparatory phase, is applied to the experimental TDR response, as illustrated in Figure 13. As shown in the figure, the classifier predicts the class L25open with a confidence level of 96.9%, indicating that branches L_2 and L_5 are affected by hard open-circuit faults.

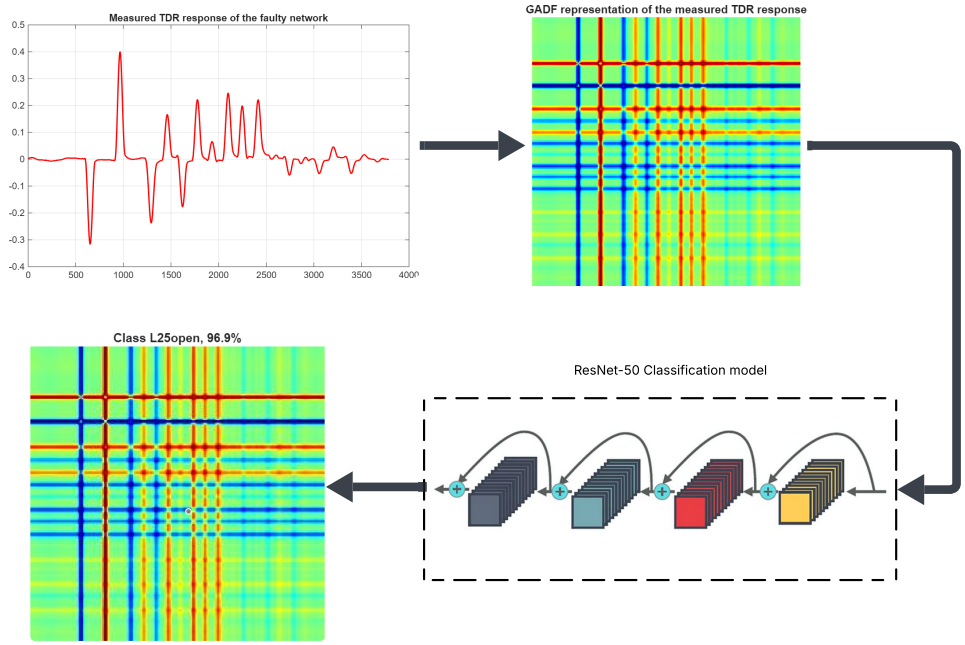


Figure 13. Online diagnosis of the obtained experimental TDR response.

Subsequently, fault localization is carried out using the multi-output ResNet-50 regression model, which estimates the effective lengths of the affected branches. The faults are localized at 0.37 m along branch L_2 and 0.38 m along branch L_5. The reconstructed wiring network incorporating the identified faults is presented in Figure 14.

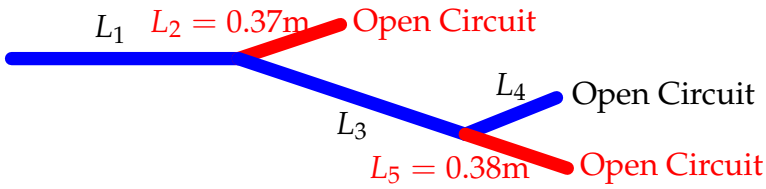


Figure 14. The YY-shaped wiring network reconstructed based on the detected faults.

To validate the applicability of the proposed framework for online diagnosis, its baseline processing capabilities and hardware requirements were evaluated. Performance tests were conducted on a standard system equipped with an Intel Core i7-10510U CPU and an NVIDIA GeForce MX250 GPU. The analysis revealed a model memory footprint of 88.08 MB, which suggests potential compatibility with the storage constraints of modern high-end embedded systems. Furthermore, the average inference time per sample was measured at 44.5 ms on the CPU and 30.4 ms on the GPU. While these processing times indicate a favorable balance between accuracy and computational efficiency, true real-time fault diagnosis on edge devices (e.g., FPGAs or edge AI accelerators) requires specific hardware optimization and validation, which will be the focus of our future work.

6. Conclusions

This paper presents a fault diagnosis framework that integrates TDR, GADF representations, and a ResNet-50 architecture to improve the accuracy and reliability of wiring network fault diagnosis. The originality of the proposed approach lies in the direct integration of the TDR-derived GADF images into a deep residual neural network, which allows effective feature learning from complex signal patterns. To support this framework, a forward modeling strategy was adopted to generate representative TDR responses under a wide range of fault conditions. Subsequently, these responses were transformed into GADF images and utilized to train and validate both ResNet-50 classification and regression models, forming a unified diagnostic scheme. Due to its robust architectural design and rich signal representation, the proposed TDR–GADF–ResNet-50 method achieves accurate fault detection, precise localization, and reliable fault characterization, even in complex wiring topologies. Comparative analyses conducted on the specific YY-network configuration demonstrate that the proposed approach achieves higher diagnostic precision than recent deep learning baselines. However, a current limitation of this framework is its limited scope to hard faults. Although diagnosing these severe failure modes is critical for safety-critical systems, soft faults represent a major practical challenge for predictive maintenance. Addressing this limitation is the focus of our ongoing investigations. Future research will focus on extending the proposed methodology to the diagnosis of soft faults in wiring networks. Beyond fault type, the present validation is conducted on a single network topology and on lossless cables. Power cables, whose importance is rapidly increasing in the context of aeronautical and automotive electrification, involve non-negligible resistive and dielectric losses that the current forward model does not account for. Extending the framework to this category of cables, where loss modeling becomes essential, is currently under investigation. Further studies will also examine the influence of environmental perturbations, such as electromagnetic interference, and investigate the incorporation of uncertainty-aware Bayesian neural network frameworks with residual architectures.

Author Contributions: Conceptualization, A.G. and M.K.S.; methodology, A.G., M.K.S., M.S.J. and H.R.E.-H.B.; software, A.G.; validation, A.G., M.K.S., M.S.J. and H.R.E.-H.B.; writing—original draft preparation, A.G.; writing—review and editing, M.K.S., M.S.J. and H.R.E.-H.B. All authors have read and agreed to the published version of the manuscript.

Funding: This research received no external funding.

Data Availability Statement: The data used during this study are available from the corresponding author upon reasonable request.

Conflicts of Interest: The authors declare that they have no conflicts of interest.

References

1. Furse, C.; Chung, Y.; Lo, C.; Pendayala, P. A critical comparison of reflectometry methods for location of wiring faults. *Smart Struct. Syst.* **2006**, *2*, 25–46. [CrossRef]
2. Abu-Rub, O.; Khan, Q.; Refaat, S.; Nounou, H. Cable insulation fault identification using partial discharge patterns analysis. *IEEE Can. J. Electr. Comput. Eng.* **2021**, *45*, 31–41. [CrossRef]
3. Zhang, H.; Mu, H.; Lu, X.; Tian, J.; Zou, X.; Zhang, G. A method for locating and diagnosing cable abrasion based on broadband impedance spectroscopy. *Energy Rep.* **2022**, *8*, 1492–1499. [CrossRef]
4. Gao, C.; Wang, L.; Mao, J.; Hu, S.; Zhang, B.; Yang, S. Non-intrusive cable fault diagnosis based on inductive directional coupling. *IEEE Trans. Power Deliv.* **2019**, *34*, 1684–1694. [CrossRef]
5. Furse, C.; Smith, P.; Safavi, M.; Lo, C. Feasibility of spread spectrum sensors for location of arcs on live wires. *IEEE Sens. J.* **2005**, *5*, 1445–1450. [CrossRef]
6. Qu, S.; Xu, Y.; Huang, S.; Sun, M.; Wang, C.; Shang, Y. Recent advancements in optical frequency-domain reflectometry: A review. *IEEE Sens. J.* **2022**, *23*, 1707–1723. [CrossRef]

7. Shi, Y.J. Theory and Application of Time-Frequency Analysis to Transient Phenomena in Electric Power and Other Physical Systems. Doctoral Dissertation, The University of Texas at Austin, Austin, TX, USA, 2004.
8. Chilan, M.; Pirhadi, A.; Asadi, S.; Helfert, S. Analysis of multiconductor transmission lines using the time domain method of lines. *Aeu-Int. J. Electron. Commun.* **2021**, *138*, 153863. [CrossRef]
9. Honarbakhsh, B.; Asadi, S. Analysis of multiconductor transmission lines using the CN-FDTD method. *IEEE Trans. Electromagn. Compat.* **2017**, *1*, 184–192. [CrossRef]
10. de Paulis, F.; Boudjefdjouf, H.; Bouchekara, H.; Orlandi, A.; Smail, M. Performance improvements of wire fault diagnosis approach based on time-domain reflectometry. *IET Sci. Meas. Technol.* **2017**, *11*, 538–544. [CrossRef]
11. Clayton, R. *Analysis of Multiconductor Transmission Lines*, 2nd ed.; John Wiley & Sons: Hoboken, NJ, USA, 2008.
12. Osman, O.; Sallem, S.; Sommervogel, L.; Carrion, M.O.; Bonnet, P.; Paladian, F. Distributed reflectometry for soft fault identification in wired networks using neural network and genetic algorithm. *IEEE Sens. J.* **2020**, *20*, 4850–4858. [CrossRef]
13. Laib, A.; Chelabi, M.; Terriche, Y.; Melit, M.; Boudjefdjouf, H.; Ahmed, H.; Chedjara, Z. Enhanced complex wire fault diagnosis via integration of time domain reflectometry and particle swarm optimization with least square support vector machine. *IET Sci. Meas. Technol.* **2024**, *18*, 417–428. [CrossRef]
14. Taki, N.; Delpha, C.; Diallo, D.; Hassen, W.B.; Ravot, N. Soft fault diagnosis in wiring networks using reflectometry and Principal Component Analysis. *Measurement* **2022**, *198*, 111378. [CrossRef]
15. Osman, O.; Sallem, S.; Sommervogel, L.; Olivas, M.; Peltier, A.; Bonnet, P.; Paladian, F. Distributed sensor diagnosis in complex wired networks for soft fault detection using reflectometry and neural network. In Proceedings of the 2019 IEEE AUTOTESTCON, National Harbor, MD, USA, 26–29 August 2019; IEEE: New York, NY, USA; pp. 1–6.
16. Goudjil, A.; Smail, M. Wiring Network Diagnosis Using Reflectometry and Twin Support Vector Machines. *Sustainability* **2025**, *17*, 1836. [CrossRef]
17. Goudjil, A.; Smail, M.; Pichon, L.; Bouchekara, H.; Javaid, M. Wiring networks diagnosis using K-Nearest neighbour classifier and dynamic time warping. *Nondestruct. Test. Eval.* **2024**, *39*, 2888–2905. [CrossRef]
18. Goudjil, A.; Smail, M.; Nahas, M. An End-to-End Approach Based on a Bidirectional Long Short-Term Memory Neural Network for Diagnosing Wiring Networks Using Reflectometry. *Sustainability* **2025**, *17*, 6241. [CrossRef]
19. Goudjil, A.; Smail, M.; Bouchekara, H.; Pichon, L.; Pouliquen, M.; Pigeon, E. A novel approach to wiring network diagnosis utilizing time domain reflectometry and one-dimensional convolutional neural networks. *Neural Comput. Appl.* **2025**, *37*, 19423–19444. [CrossRef]
20. Smail, M.K.; Bihan, Y.L.; Pichon, L. Fast diagnosis of transmission lines using neural networks and principal component analysis. *Int. J. Appl. Electromagn. Mech.* **2012**, *39*, 435–441. [CrossRef]
21. Hagness, S.; Taflove, A. *Computational Electrodynamics: The Finite-Difference Time-Domain Method;* Artech House: Norwood, MA, USA, 2000.
22. Smail, M.; Pichon, L.; Olivas, M.; Auzanneau, F.; Lambert, M. Detection of defects in wiring networks using time domain reflectometry. *IEEE Trans. Magn.* **2010**, *46*, 2998–3001. [CrossRef]
23. Lu, S.; Gao, Z.; Xu, Q.; Jiang, C.; Zhang, A.; Wang, X. Class-imbalance privacy-preserving federated learning for decentralized fault diagnosis with biometric authentication. *IEEE Trans. Ind. Inform.* **2022**, *18*, 9101–9111. [CrossRef]
24. Xie, T.; Xu, Q.; Jiang, C.; Lu, S.; Wang, X. The fault frequency priors fusion deep learning framework with application to fault diagnosis of offshore wind turbines. *Renew. Energy* **2023**, *202*, 143–153. [CrossRef]
25. Ruan, D.; Wang, J.; Yan, J.; Gühmann, C. CNN parameter design based on fault signal analysis and its application in bearing fault diagnosis. *Adv. Eng. Inform.* **2023**, *55*, 101877. [CrossRef]
26. Cui, D.; Zhou, R.; Li, H.; Hua, R.; Chen, Z.; Liu, H.; Dong, L.; Cheng, Z.; Wang, X. Rotor fault diagnosis of centrifugal pumps in nuclear power plants based on CWGAN-GP-CNN for imbalanced dataset. *Prog. Nucl. Energy* **2025**, *178*, 105500. [CrossRef]
27. Haruna, Y.; Qin, S.; Chukkol, A.; Yusuf, A.; Bello, I.; Lawan, A. Exploring the synergies of hybrid convolutional neural network and Vision Transformer architectures for computer vision: A survey. *Eng. Appl. Artif. Intell.* **2025**, *144*, 110057. [CrossRef]
28. Zhao, X.; Wang, L.; Zhang, Y.; Han, X.; Deveci, M.; Parmar, M. A review of convolutional neural networks in computer vision. *Artif. Intell. Rev.* **2024**, *57*, 99. [CrossRef]
29. Nagamani, M.; Kumar, C. Design of an improved graph-based model for real-time anomaly detection in healthcare using hybrid CNN-LSTM and federated learning. *Heliyon* **2024**, *10*, e41071. [CrossRef]
30. Soomro, D.; ChengLiang, W.; Ashraf, M.; AlHammadi, D.; Alsubai, S.; Medaglia, C.; Innab, N.; Umer, M. Automated dual CNN-based feature extraction with SMOTE for imbalanced diabetic retinopathy classification. *Image Vis. Comput.* **2025**, *159*, 105537. [CrossRef]
31. Krizhevsky, A.; Sutskever, I.; Hinton, G. ImageNet classification with deep convolutional neural networks. *Commun. Acm* **2017**, *60*, 84–90. [CrossRef]
32. Simonyan, K.; Zisserman, A. Very deep convolutional networks for large-scale image recognition. *arXiv* **2014**, arXiv:1409.1556.

33. He, K.; Zhang, X.; Ren, S.; Sun, J. Deep residual learning for image recognition. In Proceedings of the IEEE Conference on Computer Vision and Pattern Recognition, Las Vegas, NV, USA, 27–30 June 2016; pp. 770–778.
34. Shafiq, M.; Gu, Z. Deep residual learning for image recognition: A survey. *Appl. Sci.* **2022**, *12*, 8972. [CrossRef]
35. Koonce, B. ResNet 50. In *Convolutional Neural Networks with Swift for Tensorflow: Image Recognition and Dataset Categorization*; Springer: Berlin/Heidelberg, Germany, 2021; pp. 63–72.

Disclaimer/Publisher's Note: The statements, opinions and data contained in all publications are solely those of the individual author(s) and contributor(s) and not of MDPI and/or the editor(s). MDPI and/or the editor(s) disclaim responsibility for any injury to people or property resulting from any ideas, methods, instructions or products referred to in the content.